Plasma Plume Characterization of a 100 kW Nested Hall Thruster

Scott J. Hall,* Benjamin A. Jorns,† and Alec D. Gallimore‡
University of Michigan, Ann Arbor, Michigan 48109
and
Hani Kamhawi§ and Wensheng Huang¶
NASA Glenn Research Center, Cleveland, Ohio 44135

https://doi.org/10.2514/1.B38081

The plasma plume properties of a three-channel 100-kW-class nested Hall thruster were measured on xenon propellant for total powers up to 80 kW. The thruster was throttled through all seven available channel combinations for conditions spanning 300 to 500 V discharge voltage and three discharge current densities. A plasma diagnostics array, which included a Wien filter spectrometer, a retarding potential analyzer, and a planar Langmuir probe, was placed in the far-field plume of the thruster and used to measure the beam ion charge state, the ion energy distribution function, and the local plasma potential. These data were used to calculate thruster phenomenological efficiencies. These efficiencies are compared across the discharge voltage and channel combination, and they are compared to similar results from the NASA-300M single-channel high-power Hall thruster. An estimate of cross-channel ingestion, which is a phenomenon in the nested configuration that may improve thruster efficiency and that will be present in space, is calculated, and the results for mass utilization efficiency are corrected for this effect. These plasma diagnostic results are discussed in the context of the state of the art, as well as in that of the viability and potential benefits of the nested channel thruster configuration.

Nomenclature

A	=	area, cm^2
e	=	elementary charge; 1.602×10^{-19} C
I	=	current, A
j	=	current density, mA/cm^2
k_b	=	Boltzmann constant; 1.38×10^{-23} J/K
m	=	mass, kg
$\dot{m}$	=	mass flow rate, mg/s
n	=	density, m^{-3}
P	=	power, kW
T	=	thrust, N, or temperature, K
u	=	velocity, m/s
V	=	voltage, V
Z	=	charge state
α	=	portion of mass utilization efficiency related to charge state information
γ	=	cross-channel ingestion geometry factor
ζ	=	ion species fraction
η	=	efficiency
θ	=	beam divergence angle, deg
Φ	=	particle flux, particles/m^2
Ω	=	ion species current fraction

Subscripts

a	=	anode
acc	=	acceleration
act	=	actual
avg	=	average
b	=	current utilization, beam, or background
bd	=	divergence-weighted current utilization
cg	=	cathode to ground
ch	=	channel
$corrected$	=	corrected
d	=	divergence
e	=	exhaust
$facility$	=	facility
g	=	gas
i	=	species indication
$ingest$	=	ingested
k	=	species indication
lab	=	laboratory
m	=	mass utilization
md	=	divergence-weighted mass utilization
mp	=	most probable
NHT	=	nested Hall thruster
p	=	plasma potential
pc	=	power corrected
$prop$	=	propellant
q	=	charge utilization
ref	=	reference value
$space$	=	space
v	=	voltage utilization
Xe	=	xenon
$300M$	=	NASA-300M thruster

Received 18 April 2020; revision received 10 May 2021; accepted for publication 17 May 2021; published online 29 July 2021.

*Ph.D. Candidate, Department of Aerospace Engineering; currently Research Engineer, Electric Propulsion Systems Branch, HX5, LLC, NASA Glenn Research Center, Cleveland, OH 44135; scott.j.hall@nasa.gov. Member AIAA.

†Assistant Professor, Department of Aerospace Engineering; bjorns@umich.edu. Senior Member AIAA.

‡Robert J. Vlassic Dean of Engineering, Richard F. and Eleanor A. Towner Professor, and Arthur F. Thurnau Professor, Department of Aerospace Engineering; alec.gallimore@umich.edu. Fellow AIAA.

§Senior Research Engineer, Electric Propulsion Systems Branch; hani.kamhawi-1@nasa.gov. Associate Fellow AIAA.

¶Research Engineer, Electric Propulsion Systems Branch; wensheng.huang@nasa.gov. Associate Fellow AIAA.

I. Introduction

ELECTRIC propulsion (EP) systems in excess of 300 kW system power enable a wide variety of missions. Modeling has shown that systems consisting of thrusters in the 100 kW class can be optimal for both total system mass and cost for missions of at least up to 1 MW total power [1,2]. Hall thrusters have demonstrated attractive performance (total thruster efficiency in excess of 0.60)

in the range of 1500–3000 s specific impulse [3], which is an optimal range for many cargo and crew transport missions to locations such as the moon and Mars.

Using established scaling laws for Hall thrusters [4,5], single-channel thrusters begin to become challengingly large in diameter beyond the 50 kW class. An alternative geometry for Hall thrusters consists of nesting multiple discharge channels concentrically. Originally studied in two-channel 10 kW class thrusters [6,7], the concept of the nested Hall thruster (NHT) has since been scaled to the 100 kW class in the three-channel thruster known as the X3.

The X3's three channels are able to operate separately or together in any combination to provide a total throttle range on the thruster of approximately 2 to 200 kW, spanning discharge voltages from 200 to 800 V. Early testing with the thruster operated it to low powers (up to 30 kW). These tests showed lower than expected performance [2]. A series of checkouts and improvements to the thruster were made, and the thruster was recently tested up to 102 kW. The performance results (as measured by a thrust stand), as well as high-speed discharge behavior as measured with a high-speed camera, are presented by Hall in Ref. [8]. This paper presents the plasma plume characterization using a far-field array of plasma diagnostics. These measurements were taken for across nearly all of the performance characterization throttle table in Ref. [8], but damage to the probe array at the highest-power conditions prevented us from collecting these plasma plume measurements for total discharge powers above 80 kW.

First, in Sec. II, we summarize the phenomenological efficiency analysis method as applied to Hall thrusters. We present a summary of the experimental apparatus and data analysis techniques used in this experiment in Sec. III. Results from the plasma diagnostics are presented in Sec. IV, and a detailed discussion of these results is presented in Sec. V. We finally present a study of the cross-channel ingestion unique to NHTs and the correction to our results necessary because of this effect in Sec. VI.

II. Hall Thruster Phenomenological Efficiency Analysis

Direct thrust measurements via a thrust stand can be used to calculate thruster efficiency and specific impulse (both anode and total quantities of each). Such results for the X3 characterization campaign are presented in Ref. [8]. However, by using an array of plasma diagnostics in the plume of the thruster, the thruster efficiency can be subdivided into relevant quantities related to physical processes occurring within the thruster discharge. These results can be used to understand specific loss mechanisms at work within the thruster.

A significant body of work exists exploring ways to perform such an analysis [9–13]. Dissecting thruster performance in this manner provides insight into how the plasma processes change with changes in thruster operating parameters such as the discharge voltage and propellant flow rate. This type of analysis can aid with targeted thruster design improvements, as was the case with the development of the plasma lens magnetic field topography [11,14].

A. Traditional Phenomenological Efficiency Analysis

A five-component phenomenological efficiency model is often used in Hall thruster performance analysis [12]. The five components of this model are charge utilization efficiency η_q, voltage utilization efficiency η_v, current utilization efficiency η_b, mass utilization efficiency η_m, and plume divergence utilization efficiency η_d. The product of these five efficiency components is the anode efficiency:

$$\eta_a = \eta_q \eta_v \eta_b \eta_m \eta_d \tag{1}$$

and each of the components is calculated as follows:

$$\eta_q = \frac{(\sum(\Omega_i/\sqrt{Z_i}))^2}{\sum(\Omega_i/Z_i)} = \frac{(\sum(\Omega_i/\sqrt{Z_i}))^2}{\alpha_m} \tag{2}$$

$$\eta_v = \frac{V_{\text{acc}}}{V_d} \tag{3}$$

$$\eta_b = \frac{I_b}{I_d} \tag{4}$$

$$\eta_m = \frac{\dot{m}_b}{\dot{m}_a} = \alpha_m (m_{\text{Xe}} I_b / \dot{m}_a e) \tag{5}$$

$$\eta_d = (\cos\theta)^2 \tag{6}$$

where Ω_i is the current fraction of the ith species, Z_i is the charge state of the ith species, α_m is the portion of mass utilization efficiency related to the charge state information, V_{acc} is the acceleration voltage, V_d is the discharge voltage, I_b is the beam current, I_d is the discharge current, $\dot{m}_b$ is the ion beam mass flow rate, m_{Xe} is the mass of xenon, e is the elementary charge, and θ is the divergence angle of the beam.

These efficiency parameters are typically studied in the laboratory using an array of plasma diagnostics in the thruster plume [7,10,11,15,16] that includes Langmuir probes, retarding potential analyzers, Wien filter spectrometers (also called ExB probes), and Faraday probes. More about these plasma diagnostics and the computations necessary to calculate the efficiency parameters is presented in the following.

B. Limited-Diagnostics Phenomenological Efficiency Model

Early Hall thruster phenomenological efficiency analysis work such as that by Hofer and Gallimore [11] did not include η_d as in Eq. (6). Instead, diagnostics were coupled with thrust-stand-based performance measurements, which provided anode efficiency η_a; and the beam current I_b was solved for as the only unknown in the system. It was only later that η_d was explicitly added as a separate term.

The plasma diagnostic arm for the high-power X3 testing was limited to spatially static (nonmoving) probes; as such, we were unable to include a Faraday probe for ion beam current measurements. Faraday probes provide I_b and θ measurements. To provide phenomenological efficiency analysis with this setup, we revert to a model more like that of Hofer's early work [11] but with the beam divergence explicitly called out (although not solved for).

If we substitute Eqs. (2–6) into Eq. (1) and rearrange for the two unknowns (I_b and θ), we find:

$$I_b \cos\theta = \sqrt{\frac{\eta_a}{\eta_q \eta_v \alpha_m} \frac{I_d e \dot{m}_a}{m_{Xe}}} \tag{7}$$

which can be solved for explicitly using probe diagnostic data and thruster telemetry information. Using $I_b \cos\theta$, the mass utilization efficiency η_m and current utilization efficiency η_b can be rewritten into what we call their divergence-weighted values:

$$\eta_{md} = \left(\frac{m_{\text{Xe}} I_b \cos\theta}{\dot{m}_a e}\right) \alpha_m \tag{8}$$

and

$$\eta_{bd} = \frac{I_b \cos\theta}{I_d} \tag{9}$$

which are actually identical to those developed by Hofer and Gallimore in Ref. [11] but which explicitly note that the beam current I_b is weighted by the beam divergence angle θ. These modified efficiency values, which we call limited-diagnostic phenomenological efficiencies (LDPEs), will be calculated for the X3 using probe data collected during high-power testing.

To close this set of equations, we will rely on the anode efficiency as calculated through direct thrust measurements. Further details of this calculation are provided by Hall et al. [8].

C. Calculation of LDPEs for NASA-300M Thruster

In this work, we compare the phenomenological efficiency analysis results of the X3 to those of the NASA-300M as reported by Huang et al. [17]. In that study, the NASA-300M plume was thoroughly interrogated using a full suite of plasma diagnostics, including a swept Faraday probe. This provided the researchers with information on the $I_B \cos\theta$ term of the efficiency analysis, which was missing from the X3 analysis, and thus they were able to calculate all five utilization efficiencies separately. To make the comparison to the X3 data, we took the published data and calculated values for η_{md} and η_{bd} in the following manner:

$$\eta_{md,300M} = \eta_{m,300M}\sqrt{\eta_{d,300M}} \tag{10}$$

and

$$\eta_{bd,300M} = \eta_{b,300M}\sqrt{\eta_{d,300M}} \tag{11}$$

where $\eta_{b,300M}$, $\eta_{m,300M}$, and $\eta_{d,300M}$ are the current utilization, mass utilization, and divergence utilization reported for the NASA-300M. We then averaged these values for discharge voltage in a similar fashion as the X3 data.

III. Experimental Apparatus and Data Analysis

We performed the characterization of the X3 in Vacuum Facility 5 (VF-5) at NASA Glenn Research Center. This section provides a description of the experimental apparatus and plasma diagnostics used. Further details of the thruster and experimental apparatus are provided in Refs. [2,8].

A. X3 NHT

The X3 is a three-channel NHT designed to be capable of operation from 2 to 200 kW discharge power across a throttling range of discharge voltages from 200 to 800 V and total discharge currents up to 250 A. Each of the three channels of the X3 can be operated separately or together, which provides the wide throttling range of the device through seven unique operating configurations. Throughout this paper, we refer to the operating configuration by using I for the innermost channel, M for the middle channel, and O for the outermost channel. Channel combinations are then described using letter combinations, e.g., IMO for the condition where all three channels are operating simultaneously. Here, the thruster was operated on 99.9995% pure xenon propellant.

The X3 uses a single lanthanum hexaboride hollow cathode designed for operation in excess of 300 A. The cathode features unique external gas injectors that serve to reduce the energetic ion population in the near plume of the cathode [18]. As described by Goebel and Chu [19] and by Hall [20], the cathode flow is split between the cathode center and the external injectors. For the operation described here, the cathode was operated at a total cathode flow fraction (combined cathode center flow and injector flow) of 7% of the total anode flow rate across all operating channels. Elsewhere, lower cathode flow fractions were demonstrated with the X3 and this cathode; but, for the testing described here, a more conservative 7% fraction was selected as a better comparison to state of the art [20].

During this characterization, we operated the X3 through a throttle table spanning a 300–500 V discharge voltage and three discharge current densities. Normalized to the middle value, the three current densities were 0.63, 1.00, and 1.26. At each combination of discharge voltage and current density, all seven channel combinations (I, M, O, IM, IO, MO, and IMO) were tested. All operating channels were held at the same discharge voltage and current density for any given test point. Altogether, the number of unique test conditions was 46: the same throttle table for which the performance and high-speed behavior of the thruster were reported on in Ref. [8].

B. Vacuum Facility and Test Equipment

A schematic of the experimental apparatus inside VF-5 is shown in Fig. 1. The facility is a 4.6-m-diameter 18.3-m-long cylindrical vacuum chamber that provides a xenon pumping speed of 700,000 l/s. The cryogenic vacuum pumps and facility walls are lined with graphite panels, which minimize backsputter during thruster operation. As depicted in the figure, the facility pressure was monitored using a hot-cathode ionization gauge mounted in the exit plane of the thruster, approximately 1.5 m from the thruster centerline, conforming to industry best practices [21]. The gauge was calibrated on xenon and corrected for orientation. Orientation-corrected background pressures while firing the thruster ranged from 4.3×10^{-6} to 4.2×10^{-5} torr, whereas facility base pressures were typically on the order of 1×10^{-7} torr. more detailed description of the apparatus used to operate the thruster and measure telemetry was provided in Refs. [2,8].

C. Thrust Stand

We used an inverted-pendulum thrust stand designed specifically to accommodate the high thrust and large mass of the X3. This stand, which was designed to measure up to 8 N of thrust, operated in null mode and was calibrated in situ with a series of known masses. The stand had active inclination control and was water cooled to limit

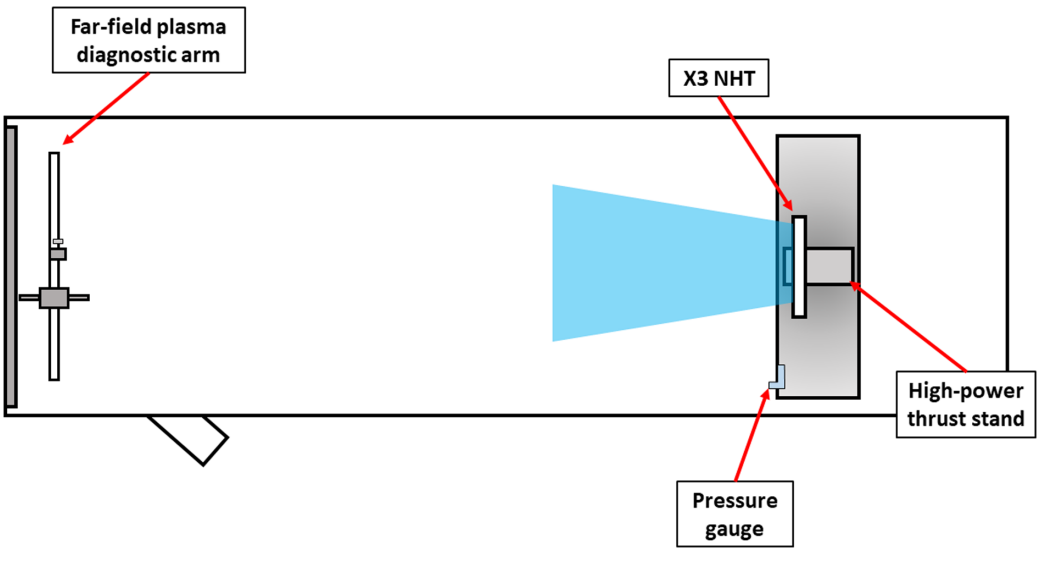

Fig. 1 Schematic of the experimental apparatus for this characterization. Drawing is not to scale.

thermal drift during thruster operation. Calibration and thrust calculation were performed following industry best practices [22–24]. Statistical uncertainty of the thrust values was calculated to be approximately 2%, plus a constant offset of 14 mN uncertainty specifically due to the resolution of the inclination control.

D. Plasma Plume Diagnostics

We used a stationary far-field plasma diagnostics package to evaluate basic plasma plume properties of the X3. The package was positioned 8.7 m from the exit plane of the thruster, near the graphite beam dump mounted to the chamber end cap of VF-5. In an effort to limit setup complexity and possible failure modes, the diagnostics package was fixed to the chamber floor instead of mounted to motion stages. In this following is a description of each of the probes and the data reduction techniques we used to process the results. These techniques generally follow those described by Huang et al. [17], as does the uncertainty analysis.

1. *Retarding Potential Analyzer*

We used a retarding potential analyzer (RPA) to measure the ion energy distribution function of the plume ions. The RPA is a plasma diagnostic that uses a series of biased and swept grids to selectively collect ions of a certain energy [25]. The RPA used in this experiment features four grids and a collector: a floating grid at the entrance, an electron repelling grid that was biased to 30 V below ground, an ion selector grid that was swept from 0 V to twice the thruster discharge voltage, and the secondary electron emission repression grid that was also biased to 30 V below ground. The RPA was located approximately on thruster centerline. We biased the ion selector grid with a commercially available source meter and measured the collected current with a commercially available picoammeter. The RPA had an opening of 6.45 cm^2; but, in an effort to minimize the plasma entering the probe at higher-power conditions, this opening was reduced to 0.065 cm^2 using a GRAFOIL® shield. The acceptance angle of the RPA in this configuration was still large enough that the entire thruster was visible to the probe.

We performed data reduction of the RPA traces similar to what was described by Huang et al. [17]. First, we smoothed the raw traces using the Savitzky–Golay method [26], and then we took a numerical derivative of the collected current I_c with respect to the ion selector grid bias V_b. The negative of this derivative $(-dI_c/dV_b)$ is proportional to the ion energy distribution function if one can assume a single ion species [25]. For calculation of the thruster voltage utilization efficiency, the RPA is used to calculate the ion energy per charge. Following Huang et al. [17], an average voltage V_{avg} was used in place of the traditional most probable voltage V_{mp} as a representation of ion energy per charge that is more robust against noise.

The bias applied to the ion selection grid in the RPA was with respect to the ground. However, the voltage through which ions are accelerated out of the thruster is with respect to the far-field plasma potential. Thus, the V_{avg} value was corrected by

$$V_{\text{acc}} = V_{\text{avg}} - V_p \tag{12}$$

where, as before, V_{acc} is the acceleration voltage and V_p is the plasma potential, which was measured using the Langmuir probe described in the following. We then used acceleration voltage V_{acc} to calculate voltage utilization efficiency as defined in Eq. (3).

We found an average uncertainty on V_{avg} of ± 1.04 V for our analysis technique. The maximum uncertainty, for a particularly noisy trace, was ± 5.2 V; and the minimum was ± 0.4 V. An average uncertainty of ± 1.04 V corresponds to an average uncertainty from the RPA contribution in η_v of ± 0.003 at a 300 V discharge voltage and ± 0.002 at 500 V. These uncertainties combine with those from the Langmuir probe analysis to provide the full uncertainty of η_v.

2. *Langmuir Probe*

We used a Langmuir probe (LP) [27] to measure the plasma potential near the RPA, and thus corrected the RPA measurements. The LP was a circular planar probe featuring an 18-mm-diameter molybdenum collector area, which was positioned perpendicular to the beam direction. The LP was swept at 10 Hz from −20 V to +20 V relative to facility ground in a triangle wave using a function generator driving a bipolar power supply.

We performed data reduction using the traditional collisionless thin-sheath LP theory [27]. Typical plasma densities of 10^{14} m^{-3} and electron temperatures of 1–2 eV provided Debye lengths of less than 1 mm and mean free paths on the order of meters, justifying this approach. The analysis was concerned chiefly with the plasma potential for RPA correction, although the floating potential and electron temperature were calculated from the traces as well. Due to the binning process in the LP data analysis method, the uncertainty in V_p was ± 0.5 V at all conditions. This uncertainty contributed an additional ± 0.002 at a 300 V discharge voltage and ± 0.001 at 500 V to the uncertainty of η_v. This brings the total to ± 0.015 at 300 V and ± 0.013 at 500 V.

3. *Wien Filter Spectrometer*

A Wien filter spectrometer (WFS) or ExB probe was used to characterize the species fractions of the first four charge states of xenon in the thruster plume. The WFS features a fixed magnetic field provided by permanent magnets crossed with a variable electric field provided by bias plates. By sweeping the voltage applied to the bias plates, ions can be collected or rejected based on their charge state. We aligned the WFS with the middle channel of the X3.

WFS data were reduced using a technique similar to that described by Huang et al. [17]. We fit a curve to each of the four detectable peaks in the current versus bias voltage trace (corresponding to singly-charged xenon (Xe^+), doubly-charged xenon (Xe^{2+}), triply-charged xenon (Xe^{3+}), and quadruply-charged xenon (Xe^{4+}), respectively) and used those curve fits to calculate current and species fractions for each ion charge state. The X3 WFS traces often (but not always) showed significant peak overlap similar to what Huang et al. found with the NASA-300 MS thruster. That study found that a skew-normal distribution provided the best fits and most consistent results for both conditions with and without strong peak overlap; because of this, we selected it for the X3 data analysis. The skew-normal distribution is a Gaussian fit with an additional fit parameter controlling skewness.

The current fraction was calculated by

$$\Omega_i = \frac{I_i}{\sum_k I_k} = \frac{n_i Z_i^{3/2}}{\sum_k n_k Z_k^{3/2}} \tag{13}$$

where Ω_i is the current fraction for species i, I is the current for a given species (calculated from the area under the curve fit for the peak of that species), n is the density of a given species, Z is the charge of a given species, and the sums over k are summed over the total number of species present (always equal to four here). Similarly, the species fraction was calculated as

$$\zeta_i = \frac{n_i}{\sum_k n_k} = \frac{\Omega_i / Z_i^{3/2}}{\sum_k \Omega_k / Z_k^{3/2}} \tag{14}$$

where ζ_i is the species fraction of species i.

The spectra from the WFS are significantly influenced by charge exchange (CEX) collisions [28] between facility background neutral particles and the beam ions. We used the correction techniques detailed by Shastry et al. [13] to account for these effects. To minimize facility effects in the plume spectra, Shastry et al. recommended maintaining a "pz" factor of less than two, where p is the facility pressure in units of 10^{-5} torr and z is the distance from the thruster exit to the WFS entrance in units of meters. For chamber pressures on the order of 10–20 μtorr, the recommended probe distance from the thruster is 1–2 m. High-power operation of the X3 came with high propellant flow rates, and thus elevated chamber pressures. The chamber pressure in VF-5 during operation ranged

from 5 to 50 μtorr, producing a recommended WFS distance from the thruster on the order of 0.5–2 m. However, this range is in the near field of the 80-cm-diameter X3, and there were significant probe heating concerns, especially at high-power operation. WFS probes are especially prone to temperature issues due to their permanent magnets, which can lose their magnetic properties at temperatures above their Curie temperature. The geometry of the test setup inside VF-5 was such that the probe could not be removed from the plume when not in use. Thus, the WFS was placed with the other far-field diagnostics 8.7 m from the exit plane of the X3. Due to the farther-than-recommended distance between the X3 and the WFS, we elected to deploy Shastry et al.'s full correction model in lieu of the simplified model used in other experiments [17].

Uncertainty in the WFS results is mostly due to the uncertainty in the pressure reading used for CEX correction. Huang et al. estimates this to be approximately $\pm 15\%$ for the pressure gauges in VF-5 when conductance losses and uncompensated temperature effects are taken into account [17]. A $\pm 15\%$ variation in the facility background pressure measurement results in average uncertainties of the current fractions of ± 0.043, ± 0.037, and ± 0.005 for Xe^{+}, Xe^{2+}, and Xe^{3+}, respectively. These, in turn, correspond to an average uncertainty in η_q of 0.004.

IV. Results

The far-field plasma diagnostics described earlier in this paper were used to calculate the four LDPEs in Eqs. (2), (3), (8), and (9). These efficiencies provide insight into the overall efficiency of the thruster via the plasma processes at work within the discharge. For the X3, these quantities can also be used to further study the way the various channel combinations of the thruster differ (or not) in operation. We present these results in the following: first, as a function of discharge power; next, averaged together for each discharge voltage tested; and finally, as functions of channel combination.

A. Variation with Discharge Power

To study the overall trends of the four LDPEs, we present each as a function of thruster discharge power. First, the anode efficiency is presented in Fig. 2. Recall that in this experiment, anode efficiency was only calculated using thrust measurements. We find that anode efficiency for all but a single test condition ranges from 0.62 to 0.72 (± 0.03, illustrated with one example error bar in the plot for clarity), and that there is no clear trend present with increasing discharge power.

Next, the four LDPE components of anode efficiency are plotted in Fig. 3. Here, error bars represent the measurement uncertainty. Error bars for charge utilization efficiency are smaller than the markers.

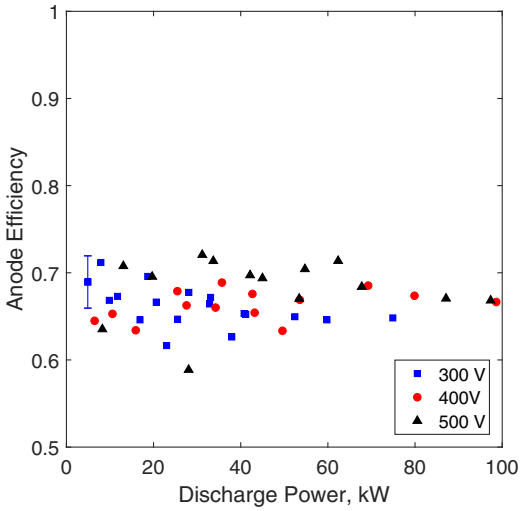

Fig. 2 Anode efficiency as a function of discharge power. A single example error bar is shown.

Charge utilization efficiency ranged from 0.97 to 0.99 (± 0.005) for all conditions, without a strong trend with increasing discharge power. Voltage utilization efficiency ranged between 0.89 and 0.98 (± 0.01) for all conditions, with all but five 300 V operating conditions above 0.93, and again with no clear trend with discharge power. Divergence-weighted mass utilization efficiency ranged from 0.84 to 1.00 (± 0.11). Here, a trend of increasing η_{md} with discharge power is observed, however, because of the large uncertainty in this measurement, this trend falls within the measurement uncertainty. Finally, the divergence-weighted current utilization ranged from 0.72 to 0.84 (± 0.11), which again was within the uncertainty of the measurement. Here, a trend of decreasing η_{bd} is seen with increasing discharge power.

B. Average Variation with Discharge Voltage

Next, we study the trends with discharge voltage. To do so, we average all test points together across all channel combinations for a given discharge voltage. This averaging will obscure trends across channel combinations operating at similar conditions, but these trends will be studied separately in Sec. IV.C below.

Figure 4 presents these averaged values versus discharge voltage. Here, error bars represent the standard deviation of the averaged data, which for all cases was smaller than the statistical uncertainty (which was omitted for clarity). Once again, error bars on η_q are smaller than the markers. As can be seen, the anode efficiency increases with increasing discharge voltage. The utilization efficiency with the lowest magnitude is η_{bd}, which matches results seen with other thrusters [11]; and it trends upward with increasing discharge voltage, contributing to the increase in anode efficiency. Average divergence-weighted mass utilization efficiency, voltage utilization efficiency, and charge utilization efficiency are all greater than 0.90 for all conditions. Voltage utilization efficiency increases with increasing discharge voltage: an expected result because the loss voltage in a Hall thruster is typically invariant with discharge voltage, and thus represents a smaller percentage at higher values of V_d. Charge utilization efficiency decreases slightly with increasing V_d, indicating an increase in the population of multiply charged ions at higher discharge voltages. This is a trend seen with the NASA-400M [29] and the NASA-173M [11] thrusters. Finally, η_{md} decreases with increasing discharge voltage; but, overall, the increase in η_v and η_{bd} is greater than this decrease and anode efficiency still increases with V_d.

C. Comparison of Channel Combinations

Finally, we analyze how the various channel combinations of the X3 operate with respect to each other. The previous sections demonstrated that, on average, the X3 is producing the expected trends and magnitudes of the various utilization efficiencies. However, it is still possible that there are differences between channels that on average cancel out to produce the results seen earlier in this paper. For instance, a certain channel could be operating more efficiently than average and another less efficiently, such that the average value appears nominal.

Here, for each channel combination, we averaged the results of a given LDPE for all 400 V discharge voltage operations. First, Fig. 5 presents the average anode efficiency for the 400 V operation for each of the seven channel combinations. As can be seen, η_a for each channel combination is the same to within the uncertainty of the measurements, and there do not appear to be any systematic trends. The similarity in η_a across channel conditions suggests that the various utilization efficiencies will be similar as well. To investigate this further, we next present each of the utilization efficiencies in turn.

First, Fig. 6a shows the variation of η_q between channel combinations. The data indicate small variations between combinations, although the previous sections have demonstrated that, in general, η_q varies little across conditions. Next, we turn to voltage utilization efficiency, as plotted in Fig. 6b. We find that η_v varies approximately 0.03 between conditions. The O, MO, and IMO configurations appear to produce slightly lower η_v than the other conditions. Figure 6c presents the divergence-weighted mass utilization as a

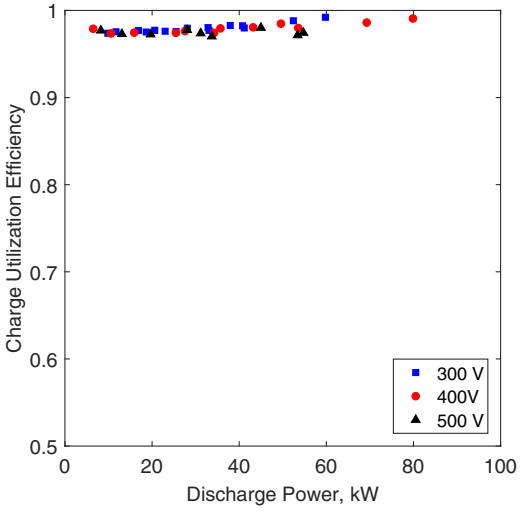

a) Charge utilization efficiency

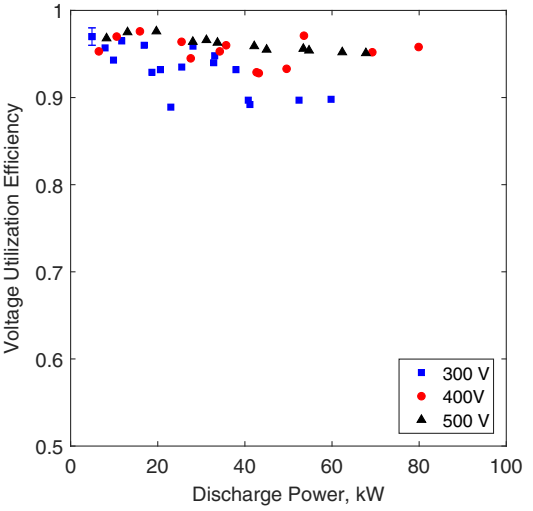

b) Voltage utilization efficiency

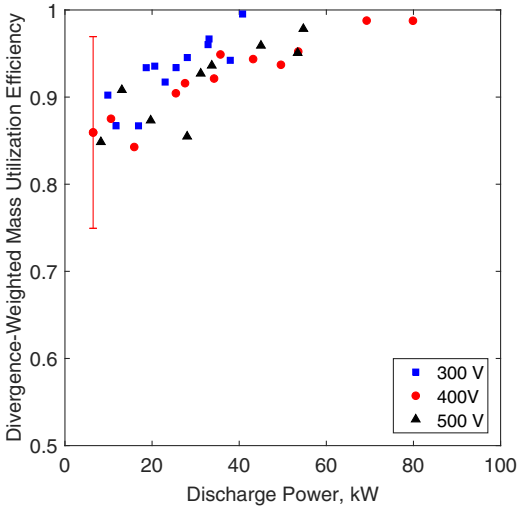

c) Divergence-weighted mass utilization efficiency

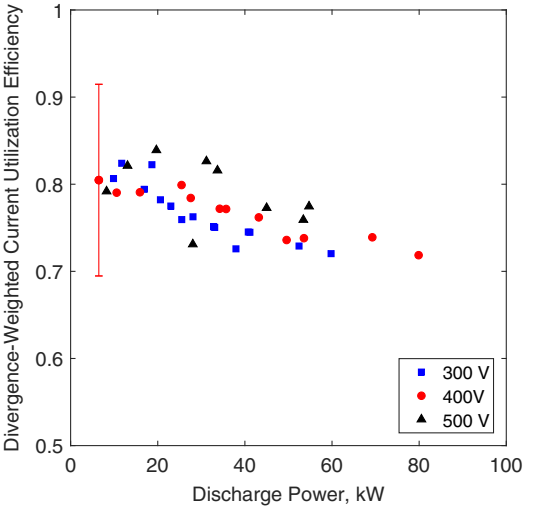

d) Divergence-weighted current utilization efficiency

Fig. 3 Limited-diagnostic phenomenological efficiencies as a function of discharge power.

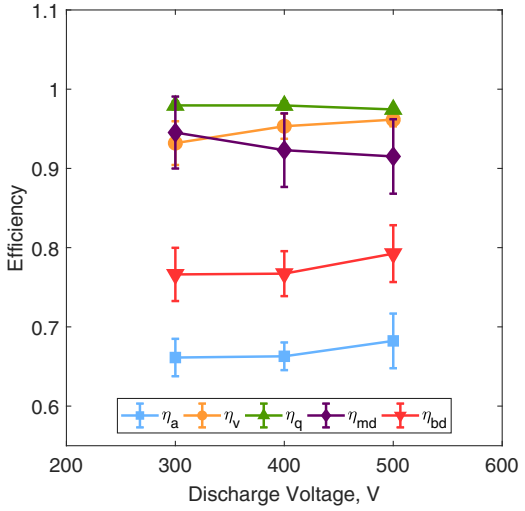

Fig. 4 The average utilization efficiencies versus discharge voltage for the X3.

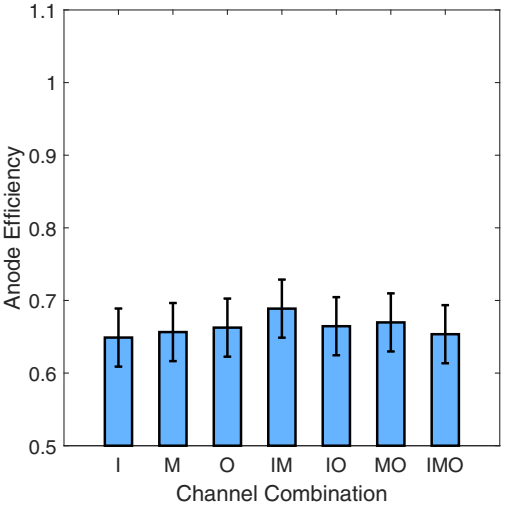

Fig. 5 Anode efficiency plotted as a function of channel combination for 400 V operation.

function of channel combination. Here, a difference among the combinations is immediately apparent, although it is within the uncertainty of the values. It appears that the single-channel conditions (in particular, the I and M conditions) operate at values of η_{md} nearly 0.10 lower than the multichannel conditions. This is a striking result when considering the parity in η_a between conditions and in all average utilization efficiencies between the X3 and the NASA-300M. The clustering of the conditions is particularly stark: the I and M conditions are within 0.006 of each other; and the IM, IO, MO, and IMO conditions are within 0.03 of each other. Yet, the two groups

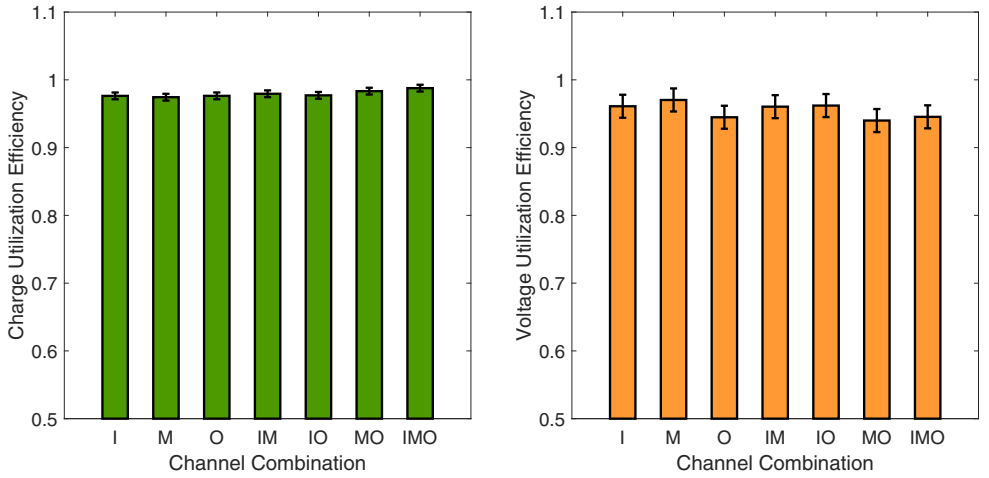

a) Charge utilization efficiency b) Voltage utilization efficiency

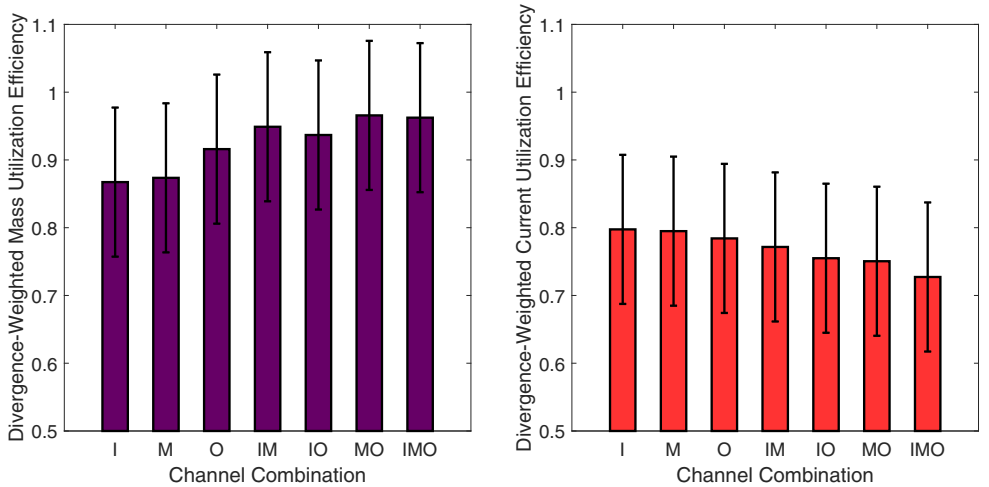

c) Divergence-weighted mass utilization efficiency d) Divergence-weighted current utilization efficiency

Fig. 6 Limited-diagnostic phenomenological efficiencies as a function of channel combination for 400 V operation of the X3 NHT.

differ on average by more than 0.08. Only the O condition falls between the two clusters. Finally, the divergence-weighted current utilization efficiency is presented in Fig. 6d. We find that the values are nearly identical at 0.79 for the I and M cases before dropping across the remaining configurations to 0.73 for the IMO condition.

V. Discussion

A. Comparison with State of the Art

We can assess the performance of the X3 by comparing its LDPE results to those of comparable state-of-the art thrusters. Here, we compare the X3's LDPE values and trends to those of the NASA-300M: a high-power nonmagnetically shielded Hall thruster, which was subject to a detailed plasma plume study.

First, we present anode efficiency, which indicates how the thrusters are performing relative to each other. As can be seen in Fig. 7, the anode efficiencies derived from thrust measurements for both thrusters track closely together with increasing discharge voltage. The X3 performed approximately 0.01 higher at 300 and 500 V, whereas the NASA-300M performed approximately 0.02 higher at 400 V. For both thrusters, anode efficiency increased for increasing discharge voltage. Also plotted in Fig. 7 are the probe-derived anode efficiencies for the NASA-300M. As can be seen, these values generally show the same trend and slope with discharge voltage but are on average 0.03 higher than the thrust-derived values.

Within the uncertainty of the X3 measurements (± 0.03), the thrust-derived anode efficiency values for both thrusters are the same. This can be taken as a confirmation that the X3 is operating as designed. Based on the scaling laws developed by Manzella in

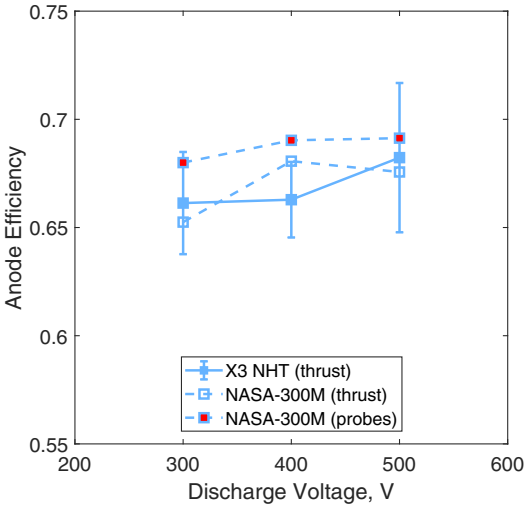

Fig. 7 Average anode efficiency as a function of discharge voltage for the X3 and the NASA-300M. Error bars on the X3 data reflect the standard deviation of the averaged points.

Ref. [4], we subsequently expect that the various utilization efficiencies should also match between the thrusters because those scaling techniques are intended to ensure that the plasma (and thus its internal processes) is kept similar as power is increased. Because the anode efficiency values are very similar, any deviations in the various utilization efficiencies will have to cancel out.

Next, we turn to the four LDPEs, which we plot for both thrusters in Fig. 8. For charge utilization efficiency, shown in Fig. 8a, results for both thrusters are nearly identical in magnitude and feature a similar negative slope with increasing discharge voltage. These values also match historical ones such as those reported by Hofer and Gallimore on the NASA-173M [11]. The results indicate that the relative populations of charge states of xenon ions are similar between the thrusters at a fixed discharge voltage. The negative slope indicates that higher discharge voltages are producing more multiply charged xenon ions. Overall, this result indicates that the X3 is not producing significantly different populations of multiply charged ions than the NASA-300M.

Voltage utilization efficiency is plotted in Fig. 8b. Here, we find that the X3 marginally outperformed the NASA-300M by 0.005–0.01 at each discharge voltage. However, the uncertainty of the X3 values were between ± 0.01 and ± 0.02, making the values statistically the same to the NASA-300M values. The results demonstrate similar trends with increasing discharge voltage between the two thrusters. This is to be expected, as discussed earlier in this paper. The similarity between these data for the two thrusters indicates that they are accelerating ions (as well as coupling to their respective cathodes) with similar efficacy.

Figure 8c presents divergence-weighted mass utilization efficiency versus discharge voltage for both thrusters. Here, we find a more striking difference between the two thrusters. Although the two thrusters show a similar downward trend in η_{md} with increasing discharge voltage, the X3's average efficiencies are consistently between 0.035 and 0.05 lower than those of the NASA-300M. This difference is not technically statistically significant because the η_{md} values for the X3 also carry an uncertainty of ± 0.11, but the difference is still significantly larger than those observed on any other efficiency. This result initially seems at odds with the similarity in all other efficiencies between the two thrusters. However, if we return to the anode efficiencies in Fig. 7, we are reminded that the probe-calculated anode efficiency for the NASA-300M was higher than the thrust-calculated value. The NASA-300M's larger η_{md} is counteracted by the X3's slightly larger η_v to result in probe-calculated anode efficiencies about 0.03 larger than the thrust-calculated ones for the NASA-300M. It is worth noting that the data for the NASA-300M produced surprisingly large values of η_m at times slightly in excess of unity. The uncertainties on the values for the NASA-300M were ± 0.04. Thus, although the difference in magnitude appears large, the uncertainties of the two measurements overlap.

Finally, Fig. 8d shows divergence-weighted current utilization efficiency. Here, we find that once again the X3 and NASA-300M data track closely. Because of the nature of the calculation for η_{bd} for the X3, it features a rather large uncertainty of ± 0.11, but the mean values are always within 0.02 between the two thrusters for a given discharge voltage. Both thrusters show an increase with increasing discharge voltage as well. This indicates that the thrusters are converting discharge current to beam current equally efficiently.

A final comparison to make to the NASA-300M is that of current fractions of charged species. The similarity in η_q between the two thrusters indicates that the relative populations should be similar as well, but it is still insightful to study trends in relative populations with V_d.

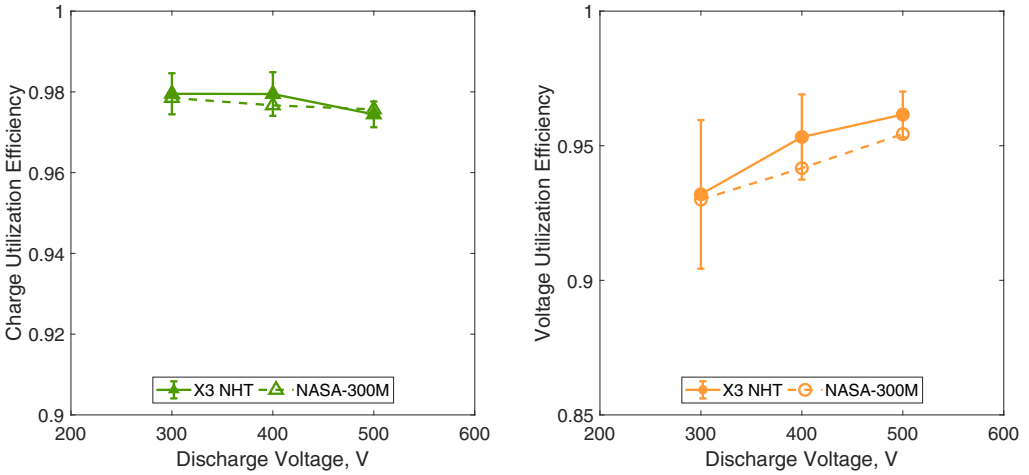

a) Charge utilization efficiency

b) Voltage utilization efficiency

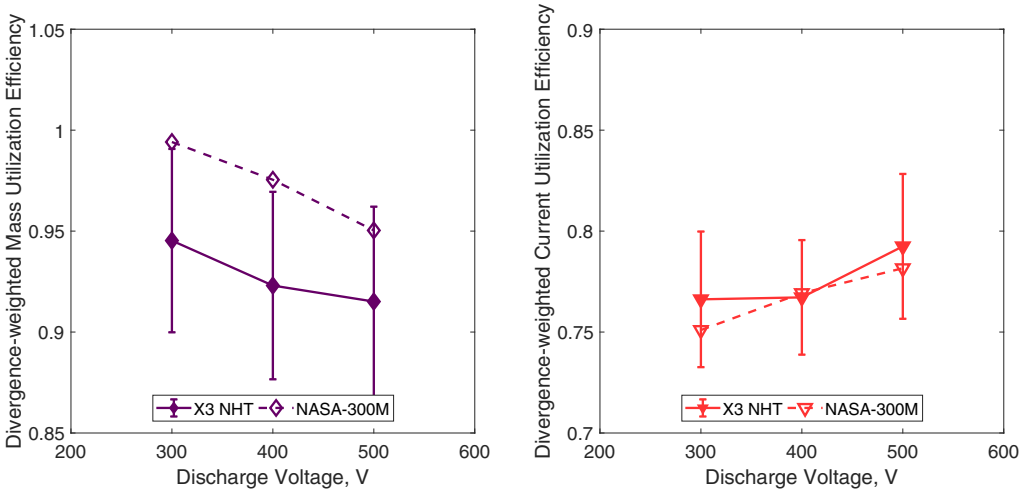

c) Divergence-weighted mass utilization efficiency

d) Divergence-weighted current utilization efficiency

Fig. 8 Limited-diagnostic phenomenological efficiencies as a function of discharge voltage for both the X3 NHT and the NASA-300M. Error bars on the X3 data reflect the standard deviation of the averaged points.

These results for the X3 and the NASA-300M are plotted in Fig. 9. Here, error bars on the X3 data represent the statistical uncertainty in the current fractions. The NASA-300M results had very similar uncertainties, which are suppressed on the plot for clarity.

We find that the NASA-300M produced magnitudes and trends very similar to the X3, as shown with the dashed lines and open markers in Fig. 9. Work such as Hofer and Gallimore's in Ref. [11] has shown that, in general, Hall thrusters experience an increase in multiply charged species populations with increasing V_d. However, for the X3 (solid lines and markers in the figure), we find that the population of Xe^+ actually increases from 0.755 at 300 V to 0.770 at 400 V before dropping to 0.712 at 500 V. This trend is mirrored in the Xe^{2+} current fraction, which decreases from 0.218 at 300 V to 0.195 at 400 V before increasing to 0.238 at 500 V. The Xe^{3+} population, which had an average current fraction less than 0.05 for all V_d, rose monotonically with discharge voltage from 0.021 at 300 V to 0.038 at 500 V. The Xe^{4+} current fraction was typically less than 0.01, and is thus not reported here.

The trends in the current fractions of all three species were very similar, with a rise in Xe^+ at 400 V and a decrease at 500 V, corresponding to a decrease in Xe^{2+} at 400 V and an increase at 500 V. The X3 and the NASA-300M produced nearly identical current fractions of Xe^+ at 300 and 400 V; although at 500 V, the X3 decreased farther than the NASA-300M. However, the magnitudes of the Xe^{2+} and Xe^{3+} populations are different between the two thrusters: the X3 is producing more Xe^{2+} and less Xe^{3+} than the NASA-300M. The X3's average current fractions for Xe^{2+} are 0.043 to 0.078 larger in magnitude than the NASA-300M, which correspond to similar differences in the opposite direction for Xe^{3+}. This, in turn, explains the X3's slightly higher magnitudes of η_q, as shown in Fig. 8; higher charge states are responsible for more losses, and so by producing more ions in a lower charge state, the X3 is operating more efficiently than the NASA-300M. However, as the difference in η_q demonstrates, this is responsible for a very small difference in performance between the two thrusters.

Aside from some reservations about divergence-weighted mass utilization, the X3 has been found to have similar magnitudes and trends for all utilization efficiencies. This suggests that the X3 is performing as it was designed to and that the thruster scaling laws used in the design of both thrusters serve to keep the plasma properties and processes similar for power levels from 20 to 100 kW and sizes ranging from approximately 300 to 800 mm in outside diameter. This also lends initial credence to the idea that the X3 does not suffer from any major changes in plasma properties and processes between single- and multichannel operations since the X3 average values here contained both types of operation and were not significantly different than the single-channel NASA-300M.

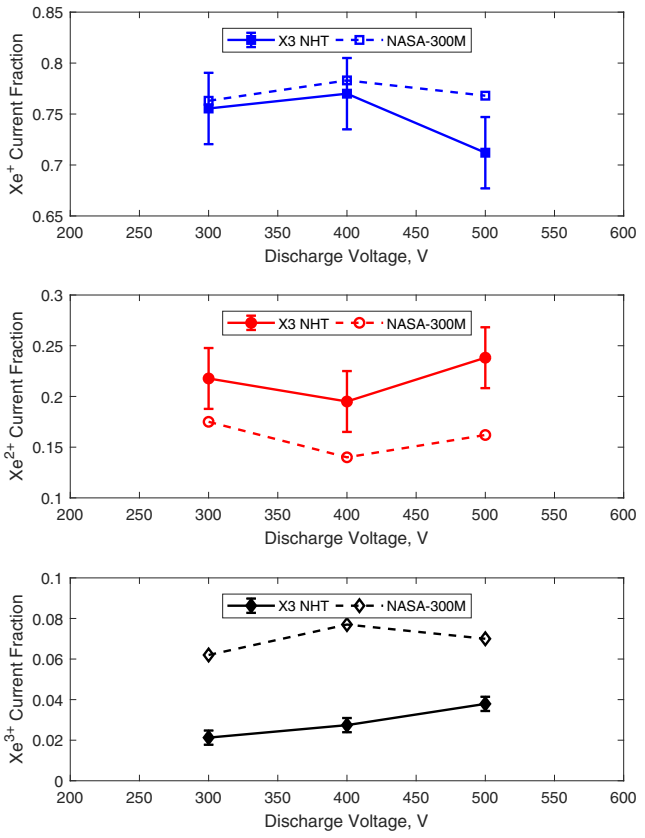

Fig. 9 Average current fractions of Xe^+, Xe^{2+}, and Xe^{3+} for the X3 and the NASA-300M at three different discharge voltages.

B. Comparison of Channel Combinations

Next, we compare the channel combinations of the X3. By doing so, we can establish whether the various combinations also operate comparably to state of the art or if there is a difference between combination(s) that averages out to roughly state-of-the-art values. We do so here for the 400 V discharge voltage conditions.

The charge utilization efficiencies of each channel combination in Fig. 6 suggest that the thruster is producing more singly charged xenon in the MO and IMO configurations. Indeed, if we plot the average current fractions of Xe^+, Xe^{2+}, and Xe^{3+} as Fig. 10 shows, we find that the MO and IMO configurations are producing more singly charged xenon ions and fewer doubly charged ions. The populations of triply charged ions remain approximately the same and are a small portion of the beam population.

As noted earlier in this paper, the O, MO, and IMO configurations produced values of η_v slightly lower than those of other conditions. One potential explanation for this is that the outer channel's lower efficiency occurs in both single- and multichannel operations, and thus brings down the average η_v for any condition that channel operates in. However, this would not explain the high η_v for the IO condition, which is on par with that for the I condition. Therefore, it is also possible that this is simply a product of magnetic field settings; further optimization of the field, especially for the multichannel conditions, may bring these values closer together.

Another possible explanation for the variation in η_v seen here is variations in either V_{cg}, V_p, or both. These two potentials are combined in the cathode coupling voltage. The data for these conditions are plotted in Fig. 11. We find that there is variation of up to 4 V in V_{cg} among conditions and up to 5 V in V_p among conditions. The variation in V_{cg} is less systematic, but V_p for the O, MO, and IMO conditions is the highest of the set. However, the increase in V_p for these sets is not coupled with similar increases in the magnitude of V_{cg}, resulting in overall loss parameters that are no more than 1–2 V higher than the rest. One notable exception is the IM condition, which features small values of both V_p and V_{cg}, although this smaller loss parameter does not translate to a detectably larger η_v. The overall

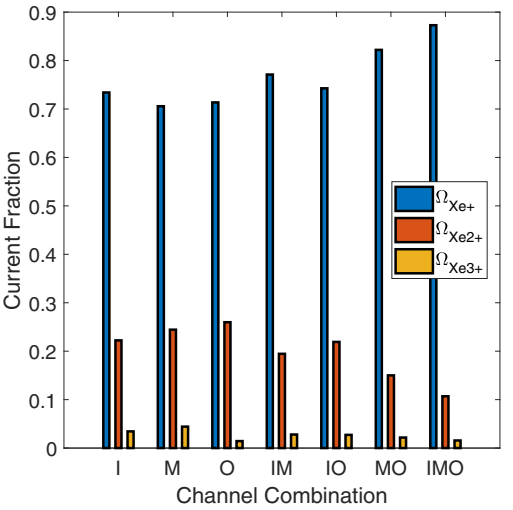

Fig. 10 The average current fractions of Xe^+, Xe^{2+}, and Xe^{3+} at 400 V discharge voltage for each X3 channel combination.

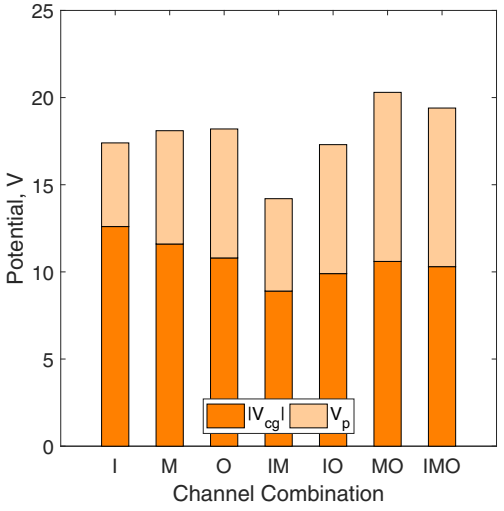

Fig. 11 The average magnitudes of V_{cg} and V_p for each channel combination at 400 V discharge voltage.

variation in the loss parameter is approximately 5 V, which is just over 1% of the discharge voltage. These results indicate that the mechanism by which η_v is lowered for certain conditions is related to the effectiveness at accelerating ions through the available potential, and not in a difference in the available potential itself.

It is interesting to note that the channel combinations that included the outer channel had larger plasma potentials than the combinations that did not. The differences were relatively small and close to the measurement uncertainty, meaning that this may not be representative of a physical trend. However, modeling work done by Mikellides and Ortega of the X3 in the Jet Propulsion Laboratory's two-dimensional axisymmetric Hall thruster simulation code Hall2De suggested that the outer channel was likely to produce higher plasma potentials than the other two channels [30]. Although this difference is strongest near the thruster, at 3.5 thruster diameters downstream (the extent of the simulations), the simulations predicted a difference of over 10 V between the outer channel's plasma potential and that of the other two channels. Here, at approximately 10 thruster diameters downstream, we typically measured plasma potentials a few volts higher for conditions that included the outer channel. Mikellides and Ortega's modeling suggested that this phenomenon was ultimately due to the magnetic field in the near-plume region of the outer channel, which is distinctly stronger there than in the other two channels. This stronger magnetic field imposes a higher plasma resistivity, which in turn causes increased electron heating and a higher electron temperature. Through the electron pressure, these higher electron temperatures correlate with higher plasma potentials. Both the simulation and experimental results are preliminary, and near-field diagnostics are certainly necessary to verify this result. Nonetheless, the initial correlation between the simulations and the laboratory results is encouraging.

Finally, as noted earlier in this paper and shown in Fig. 6d, divergence-weighted current utilization efficiency decreases when moving from single- to multichannel conditions. This decrease in η_{bd}, coupled with the trends in the other parameters (notably, η_{md}), explains how the anode efficiency could be nearly invariant for all channel combinations. This result implies that either the divergence is getting larger for the multichannel conditions or there is an increase in electron current. However, η_{md} is also weighted by $\cos\theta$ but trends in the opposite direction. This implies that this observed change in η_{bd} is not due to a change in divergence angle but instead is due to changes in electron current.

VI. Calculation of NHT Effects

A. Theory

The thrust produced by a Hall thruster is a function of the actual or total mass flow rate being processed by the discharge, which is summed over all channels:

$$T = u_e \sum_i \dot{m}_{\text{ch,act},i} \tag{15}$$

where $\dot{m}_{\text{ch},i}$ is the total flow rate being processed by channel i. This flow rate has two major sources in Hall thruster ground testing:

$$\dot{m}_{\text{ch},i} = \dot{m}_{a,i} + \dot{m}_{\text{ingest},i} \tag{16}$$

where $\dot{m}_{a,i}$ is the prescribed anode flow rate to channel i, and $\dot{m}_{\text{ingest},i}$ is the flow rate ingested by that channel by separate mechanisms: for instance, by flux to the channel from a ground-test facility with finite background pressure. The discharge power of a Hall thruster is similarly dependent on the total flow rate being processed by the channel:

$$P_d = \sum_i V_{d,i} I_{d,i} = \sum_i V_{d,i} \frac{e}{m_{\text{prop}}} \dot{m}_{\text{ch},i} \tag{17}$$

where P_d is the discharge power, $V_{d,i}$ and $I_{d,i}$ are the discharge voltage and current of channel i, e is the elementary charge, and m_{prop} is the propellant atomic mass. This is due to the fact that the discharge current is dictated by the total mass being processed by the discharge from all sources.

Both T and P_d are quantities that are measured in the laboratory. Thus, it is apparent that to properly calculate anode or total efficiency values, the proper mass flow rate to use is not simply $\dot{m}_a$ but $\dot{m}_{\text{ch}}$, which takes into account the "free" propellant not accounted for by the anode mass flow rates alone. A correction must be made to the "laboratory" anode efficiency, which only uses the anode mass flow rates in the calculation, to account for this effect. We can rewrite the expression of anode efficiency as measured in the laboratory $\eta_{a,\text{lab}}$ to accommodate this updated mass flow rate as

$$\eta_{a,\text{corrected}} = (\eta_{a,\text{lab}}) \left(\frac{\dot{m}_a}{\dot{m}_{\text{ch}}} \right) \tag{18}$$

We find that this correction factor is less than unity when there is additional propellant being ingested, which makes sense because the corrected anode efficiency value is now accounting for all propellant the thruster is processing.

1. Test Facility Ingestion

Traditionally, $\dot{m}_{\text{ingest}}$ due to facility ingestion $\dot{m}_{\text{facility}}$ is calculated as the flux to the discharge channel using kinetic theory [31–33]:

$$\dot{m}_{\text{facility}} = \Phi m_{\text{prop}} A_{\text{ingest}} = \sqrt{\frac{m_{\text{prop}}}{2\pi k_b T_g}} p_b A_{\text{ingest}} \tag{19}$$

where Φ is the particle flux, A_{ingest} is the ingestion area (here, this is the thruster discharge annular exit area), k_b is Boltzmann's constant, T_g is the gas temperature (typically taken as the anode temperature of around 500 K), and p_b is the facility background pressure.

However, tests with multiple thrusters in multiple facilities have demonstrated that Eq. (19) does not fully account for the changes seen in thruster operation with changing facility background pressure [32,33]. Recent works by Frieman et al. have demonstrated that the so-called thermal model, as Eq. (19) is referred to, is not accurate because it fails to account for the presence of bulk motion in the background gas typical of most EP test facilities [34,35]. In place of the thermal model, Frieman et al. propose a model called the background flow model that captures these bulk motion effects. Frieman et al.'s work generalizes a model originally developed by Cai [36] to accommodate a variety of facility configurations. The model was validated against a variety of experimental data and generally showed significantly improved agreement over the thermal model results. The background flow model calculates an expected flux at the plane of the thruster based on facility factors such as the cryopump temperature, surface area, sticking coefficient, and location, as well as the facility cross section. The model also accounts

for collisional scattering between the neutrals flowing toward the thruster and those flowing out of the thruster. From this expected flux, the ingested mass flow rate $\dot{m}_{\text{facility}}$ is calculated. The mathematics of the model are left to the reader in Ref. [35].

We applied the background flow model here to calculate a more accurate value of $\dot{m}_{\text{facility}}$. We used specific coefficients to represent VF-5 in the model. These values are based on the pump configuration (pump area, temperature, and location) of the facility [34]. Using this value of $\dot{m}_{\text{facility}}$ in Eq. (18), we find an expression for anode efficiency corrected for facility ingestion:

$$\eta_{a,\text{facility}} = \eta_{a,\text{lab}} \frac{\dot{m}_a}{\dot{m}_a + \dot{m}_{\text{facility}}} = \eta_{a,\text{lab}} \eta_{\text{facility}} \tag{20}$$

where we define the mass flow rate fraction as η_{facility}. This new efficiency term will be unity when no background gas is ingested and less than unity for cases with ingestion, thus correcting the anode efficiency to reflect the additional propellant mass.

2. NHT Cross-Channel Ingestion

In addition to facility ingestion, each channel of a nested Hall thruster can ingest neutral gas from other operating channels of the thruster. This is a separate effect from facility ingestion because it will still exist in space and is not a byproduct of testing in a facility with finite pumping speed. In its most general form, this NHT ingestion term $\dot{m}_{NHT}$ can be expressed as

$$\dot{m}_{\text{NHT},i} = \sum_j \gamma_{ij} \dot{m}_{a,j} \tag{21}$$

Each channel i ingests some amount of neutral flow from the other firing channels j. This ingestion from each channel is a function of that channel's flow rate $\dot{m}_{a,j}$ and a geometry factor γ_{ij}, which itself is a function of the relative ingestion areas and proximity of channel j to channel i, as well as a weighting factor accounting for whether the channel is operating or simply flowing cold gas. The summation over j should also include the cathode, which is also a source of neutral particles. This is of increased importance on thrusters such as the X3 that feature external neutral injection at the cathode.

Thus, following the aforementioned development, we can expect a similar mass flow rate fraction relating the effect of the ingestion from other channels on the anode efficiency of the thruster. However, unlike the $\eta_{facility}$ term, which should be removed from $\eta_{a,lab}$ to correct for effects not seen on orbit, the effects due to propellant sharing between channels is an effect that will be seen on orbit, and thus does not need to be removed from the ground-test thruster efficiency analysis. However, we can still separate the value and calculate it as a separate efficiency term in the phenomenological model. In this manner, we find

$$\begin{aligned} \eta_{a,\text{space}} &= (\eta_{a,\text{lab}} \eta_{\text{facility}}) \left(\frac{\sum_i \dot{m}_{a,i} + \dot{m}_{\text{facility},i} + \dot{m}_{\text{NHT},i}}{\sum_i \dot{m}_{a,i} + \dot{m}_{\text{facility},i}} \right) \\ &= \eta_{a,\text{lab}} \eta_{\text{facility}} \eta_{\text{NHT}} \end{aligned} \tag{22}$$

where we find that η_{NHT}, as it is defined, increases the effective in-space anode efficiency $\eta_{a,\text{space}}$ when the channels are ingesting from each other and is unity when there is no cross-channel neutral sharing.

Determining $\dot{m}_{\text{NHT}}$ in the laboratory can be difficult because a number of competing phenomena are at work. The ideal way to do so would be to operate each of the channel combinations at a fixed facility background pressure and magnetic field, as well as observe how the ingestion (by way of changes in the discharge current) varies between cases for a given set of discharge voltages and currents. Variations could be made in cathode flow and channel flow separately to make quantitative assessments of γ_{ij} for each combination. However, this manner of highly controlled experiment may be difficult, especially for large thrusters where the background pressures vary considerably between conditions. It must be understood that a η_{NHT} value established for a set of channel combinations at fixed discharge voltage and current but for varying background pressure and magnetic field settings likely contains effects from multiple phenomena, not all of which are exclusive to NHTs. For instance, work has shown that the discharge current oscillation level varies with facility pressure [32] and that these levels are correlated with changes in thruster performance [37]. Changes in background pressure across conditions may cause a channel to change oscillation modes, and thus change performance, resulting in an anomalous value of η_{NHT} from an apparent difference in required propellant flow rate that is not a product of cross-channel ingestion. Background pressure has also been shown to shift the location of the acceleration region within the Hall thruster discharge channel, also resulting in a change in performance and operation of the thruster [38]. These effects are difficult enough to uncouple from one another for single-channel thrusters, and the addition of multiple channels interacting with one another only increases the complexity. However, a preliminary attempt can still be made to estimate the value of η_{NHT} from thruster performance data.

It is expected that η_{facility} will be roughly constant across all conditions, and thus represent a linear offset in the data. Indeed, in calculating η_{facility} using the background flow model, we find that the average value across all test conditions during the high-power campaign was 0.987 with a standard deviation of 0.001. This slight variation in values was likely due to the exact facility conditions for the day. Additionally, because this correction is not typically undertaken in the literature, comparison with other thrusters will be more complicated with this facility ingestion correction applied.

The thruster was not operated in the perfectly controlled manner discussed earlier in this paper, meaning that background pressure-based effects on thruster oscillation mode and acceleration region location are likely captured artificially in an η_{NHT} calculation. Additionally, because this cross-channel ingestion will be present in space, and thus is a fundamental component of device operation, it should not be removed or corrected for. However, it is necessary to at least extract and study this factor to understand its role in thruster operation.

B. Procedure

The analysis of NHT cross-channel ingestion effects had three major steps: power correction, facility ingestion calculation and removal, and calculation of η_{NHT}. The various operating conditions of the X3 were not always perfectly power matched across a set (that is, target discharge currents and voltages were not always perfectly achieved). To facilitate more accurate calculations of η_{NHT}, we power corrected the flow rates of the thruster. This process was straightforward: we used the ratio of the discharge current to the anode mass flow rate ($I_d/\dot{m}$) to predict the required flow rate at the target discharge current. Maximum corrections were 1.81 mg/s for the inner channel, 3.35 mg/s for the middle channel, and 2.84 mg/s for the outer channel, with average corrections much smaller (between 0.29 and 0.50 mg/s for all three channels). These corrections allow us to compare channel conditions as though they operated at exactly the same discharge power. Although the value of $I_d/\dot{m}$ was shown to change between conditions, these power corrections are small enough that we assume $I_d/\dot{m}$ is constant for the correction range for each condition.

Using these power-corrected flow rates $\dot{m}_{pc}$, we used Frieman et al.'s background flow model [35] to calculate the neutral ingestion to the thruster at each condition. These ingestion flow rates $\dot{m}_{\text{facility}}$ were then subtracted from the $\dot{m}_{pc}$ values to isolate the "spacelike" flow rates. Using these flow rates, we calculated the apparent ingestion due to NHT effects. At a given set of configurations at a given operating condition (discharge voltage and current density), we compared multichannel flow rates to the sum of their constituent single-channel flow rates. Following Eq. (22), we use the difference in these flow rates to calculate η_{NHT} for each condition.

If ingestion of vacuum facility neutrals was the only mechanism of ingestion, the two flow rates should match, and η_{NHT} should be equal to unity. If the multichannel flow rates are larger than the

single-channel values, it indicates that there is a loss mechanism at play during multichannel operation that is requiring more propellant for the same discharge power. This would result in values of η_{NHT} less than unity. Finally, if the predicted result is true (that propellant is being ingested between channels in multichannel operation), then η_{NHT} should be greater than unity.

C. Results

Indeed, we find that for all multichannel conditions, η_{NHT} is greater than unity. Table 1 presents values for all multichannel operating conditions tested. We found that η_{NHT} varied between a minimum of 1.016 and a maximum of 1.128. We found that the various multichannel combinations demonstrated very similar average values of η_{NHT}, with the IO condition producing slightly smaller values than the others. Of all the multichannel combinations, IO is the only one where the firing channels are not directly adjacent to each other. We expect that η_{NHT} and the cross-channel ingestion is a local process, and the significant increase in distance between the channels in the IO configuration (over double that of adjacent channels) likely results in less neutral ingestion. This is reflected in these values, and it provides a hint at the difference in the γ_{ij} geometry factors for the channels that are farther apart.

The mass flow rates involved in the calculation of η_{NHT} are significantly larger than those ingested from the facility. For the 400 V, $1.0j_{\mathrm{ref}}$ condition, for example, the background flow model predicts the thruster is ingesting 1.2 mg/s for the IMO condition, yet the total difference in flow rates between that condition and the sum of the I, M, and O conditions (with their respective facility ingestion subtracted) is 7.5 mg/s. Ingestion of the facility neutrals accounts for only 16% of this flow rate deficit.

These results also have an important effect on the phenomenological efficiency analysis performed in the preceding section. Figure 6 showed that the divergence-weighted mass utilization efficiency of the multichannel configurations was notably higher than for the single-channel configurations. When we correct these values by removing η_{NHT}, we find that η_{md} for these conditions is much more alike across all channel combinations. These results are presented in Fig. 12. Whereas the uncorrected values varied by between 0.08 and 0.10 between the single channel and multichannel, with the NHT correction, variation is between 0.04 and 0.06.

As discussed earlier in this paper, the η_{NHT} effect will be present in space because it is related to ingestion of neutrals emanating from the device itself, and not those remaining due to finite facility pumping speed. However, calculation of η_a here incorporates these $\eta_{\mathrm{NHT}} > 1$ values. That is, the η_a values for multichannel operation are inflated by η_{NHT}. This must be kept in mind when comparing results with state-of-the-art single-channel thrusters.

Further work is needed to fully characterize this effect on the performance of the X3 and NHTs in general. Although the X3's performance appeared comparable to other high-power Hall thrusters, the present calculation indicates that a portion of the η_a value was likely due to NHT effects. This implies that the X3 may not be operating as efficiently as state-of-the-art single-channel thrusters in multichannel modes once these effects are controlled for. Our calculated η_{NHT} values indicate that the X3 and other NHTs should

Table 1 Values of η_{NHT} for various X3 operating conditions

V_d, V	j	*IM*	*IO*	*MO*	*IMO*
300	$0.63j_{\mathrm{ref}}$	1.016	1.057	1.070	1.095
300	$1.0j_{\mathrm{ref}}$	1.060	1.026	1.023	1.030
400	$0.63j_{\mathrm{ref}}$	— —	1.052	1.048	1.062
400	$1.0j_{\mathrm{ref}}$	1.051	1.035	1.034	1.040
500	$0.63j_{\mathrm{ref}}$	1.070	1.031	1.128	1.056
500	$1.0j_{\mathrm{ref}}$	1.057	1.030	1.029	1.041
Average		1.051	1.039	1.055	1.054
Standard deviation		0.020	0.013	0.039	0.023

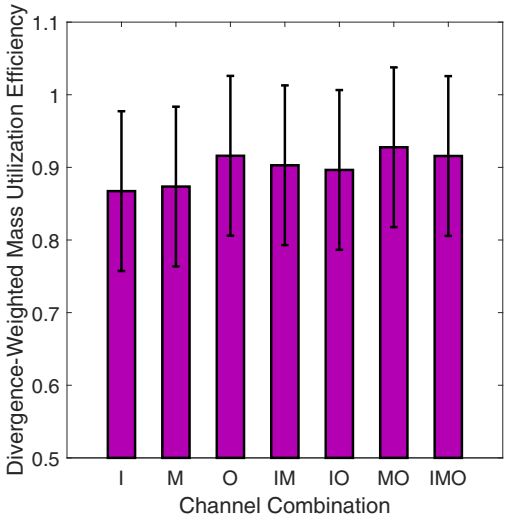

Fig. 12 Divergence-weighted mass utilization efficiency, corrected for NHT ingestion effects, plotted as a function of channel combination for 400 V operation.

be capable of operation at anode efficiencies as much as 0.05 above the state of the art when operating multiple channels. At a minimum, further magnetic field optimization is needed for multichannel operation of the X3, and it is entirely likely that a more detailed study of the fields would increase thruster performance.

D. Analysis Limitations

This experiment was not designed with measuring η_{NHT} as a primary goal; as such, the calculations done earlier in this paper are notional at best. As discussed, there are likely a number of thruster behavior differences being captured in the η_{NHT} term; and it is unclear from this test how many of those effects will be present in space. A more detailed experiment, where parameters are properly controlled with the express purpose of studying this effect, will help differentiate between ground-test facility effects and those inherent to the NHT geometry. The values reported here should be taken as maximums because they likely capture other effects as well. It is also likely that the plume structure, and thus the ingestion mechanism, may change with decreasing facility background pressure, further changing how the effects actually appear in space.

VII. Conclusions

Using a fixed far-field plasma diagnostic array consisting of a Wien filter spectrometer, a retarding potential analyzer, and a planar Langmuir probe, the phenomenological efficiency breakdown of the X3 NHT operating across total powers of 5–102 kW was studied. Results indicated that, on average, the X3 NHT was operating in a similar fashion to the NASA-300M, which is a 20-kW-class single-channel Hall thruster designed using similar scaling principles. The X3 NHT produced similar quantities and trends with increasing discharge voltage in charge utilization efficiency, voltage utilization efficiency, and divergence-weighted current utilization efficiency. The trend was very similar between the two thrusters for divergence-weighted mass utilization efficiency, but the values for the X3 NHT were, on average, 0.05 lower than for the NASA-300M. Additionally, we showed that the average current fractions of Xe^{+}, Xe^{2+}, and Xe^{3+} were similar between the two thrusters and demonstrated similar trends with increasing discharge voltage. The results indicated that the X3 NHT was producing slightly more Xe^{2+} and less Xe^{3+} than the NASA-300M, but these differences in population were not enough to cause a noticeable difference in charge utilization efficiency between the two thrusters.

We also compared the phenomenological efficiency results between the various channel combinations of the X3 NHT for 400 V operation to study the potential differences in operation between these combinations. The anode efficiency and all four

LDPEs were within their respective uncertainties for all channel combinations. However, the two divergence-weighted quantities (mass and current utilization efficiency) showed variation with channel combination that was larger than those seen for anode, charge utilization, and voltage utilization efficiency. (The uncertainty was larger for the divergence-weighted quantities because of the way they were calculated). Divergence-weighted current utilization efficiency appeared to decrease from about 0.8 ($\pm$0.11) for the I condition to 0.75 ($\pm$0.11) for the IMO condition, and divergence-weighted mass utilization efficiency increased from 0.86 ($\pm$0.11) to 0.95 ($\pm$0.11) between the same.

Finally, the effect that cross-channel ingestion between simultaneously firing channels of the X3 NHT was calculated. This is a phenomenon that will contribute to an increase in efficiency of the thruster by allowing the discharge channels to use un-ionized propellant from other channels to create thrust. However, unlike the ingestion of background gas from ground-test facilities [35], these NHT effects will be present, in some form, in space. The current calculations, which offer a preliminary look at the potential impact of these effects, showed that multichannel operating conditions appeared to be ingesting enough gas from adjacent channels to account for approximately a 5% increase in efficiency (corresponding in an increase in total thruster efficiency of approximately 0.03). For the IO condition, where the channels are separated by the nonfiring middle channel, the effect was, on average, approximately 1% lower than for the other conditions where channels were directly adjacent. These calculations were preliminary due to this characterization effort being primarily focused on other aspects of thruster operation. However, they indicate that this cross-channel ingestion has the potential to allow NHTs to operate at higher total efficiencies than single-channel thrusters. A more detailed study of the phenomenon is necessary to better understand the physics of the effect and how to capitalize on it.

Overall, it has been demonstrated that in both single- and multichannel operations, the X3 NHT produces thruster efficiencies similar to a state-of-the-art single-channel thruster: the NASA-300M. Furthermore, when the thruster efficiency is broken into phenomenological efficiencies based on plasma plume measurements, the results are also similar in magnitude and trend to those from the NASA-300M. These results suggest that nesting the channels of Hall thrusters does not fundamentally alter their operation, providing promising results for their continued development and eventual application to high-power space missions.

Acknowledgments

At the time of this work, Scott J. Hall was supported by a NASA Space Technology Research Fellowship under grant number NNX14AL67H. A portion of the work described here was performed as a part of NASA's Next Space Technologies for Exploration Partnerships (NextSTEP) program under grant number NNH16CP17C. The plasma diagnostics in this experiment were funded by a Michigan Institute of Plasma Science and Engineering Graduate Student Fellowship. The authors gratefully acknowledge Joshua M. Woods of the University of Michigan for assistance with the plasma diagnostics. The authors would like to acknowledge a number of personnel at NASA Glenn Research Center who contributed to this work, including Eric Pencil, Luis Piñero, Chad Joppeck, Taylor Varouh, Nick Lalli, Richard Senyitko, Jim Zakany, Jim Szelagowski, Kevin Blake, Josh Gibson, Larry Hambley, George Jacynycz, and Dave Yendriga. Finally, the authors gratefully acknowledge Dan M. Goebel of NASA's Jet Propulsion Laboratory for developing and providing the cathode used in this experiment, as well as for his technical insight.

References

[1] Hofer, R. R., and Randolph, T. M., "Mass and Cost Model for Selecting Thruster Size in Electric Propulsion Systems," *Journal of Propulsion and Power*, Vol. 29, No. 1, 2013, pp. 166–177. https://doi.org/10.2514/1.B34525

[2] Hall, S. J., "Characterization of a 100-kW Class Nested-Channel Hall Thruster," Ph.D. Dissertation, Univ. of Michigan, Ann Arbor, MI, 2018.

[3] Goebel, D. M., and Katz, I., *Fundamentals of Electric Propulsion: Ion and Hall Thrusters*, Wiley, Hoboken, NJ, 2008.

[4] Manzella, D., "Scaling Hall Thrusters to High Power," Ph.D. Dissertation, Stanford Univ., Stanford, CA, 2005.

[5] Dannenmayer, K., and Mazouffre, S., "Elementary Scaling Relations for Hall Effect Thrusters," *Journal of Propulsion and Power*, Vol. 27, No. 1, 2011, pp. 236–245. https://doi.org/10.2514/1.48382

[6] Szabo, J., Pote, B., Hruby, V., Byrne, L., Tedrake, R., Kolencik, G., Kamhawi, H., and Haag, T. W., "A Commercial One Newton Hall Effect Thruster for High Power In-Space Missions," *47th AIAA/ASME/SAE/ASEE Joint Propulsion Conference*, AIAA Paper 2011-6152, 2011. https://doi.org/10.2514/6.2011-6152

[7] Liang, R., "The Combination of Two Concentric Discharge Channels into a Nested Hall-Effect Thruster," Ph.D. Dissertation, Univ. of Michigan, Ann Arbor, MI, 2013.

[8] Hall, S. J., Jorns, B. A., Cusson, S. E., Gallimore, A. D., Kamhawi, H., Peterson, P. Y., Haag, T. W., Mackey, J. A., Baird, M. J., and Gilland, J. H., "Performance and High-Speed Characterization of a 100-kW Nested Hall Thruster," *Journal of Propulsion and Power* (to be published).

[9] Kim, V., "Main Physical Features and Processes Determining the Performance of Stationary Plasma Thrusters," *Journal of Propulsion and Power*, Vol. 14, No. 5, 1998, pp. 736–743. https://doi.org/10.2514/2.5335

[10] Hofer, R. R., "Development and Characterization of High-Efficiency, High-Specific Impulse Xenon Hall Thrusters," Ph.D. Dissertation, Univ. of Michigan, Ann Arbor, MI, 2004.

[11] Hofer, R. R., and Gallimore, A. D., "High-Specific Impulse Hall Thrusters, Part 2: Efficiency Analysis," *Journal of Propulsion and Power*, Vol. 22, No. 4, 2006, pp. 732–740. https://doi.org/10.2514/1.15954

[12] Brown, D. L., Larson, C. W., Beal, B. E., and Gallimore, A. D., "Methodology and Historical Perspective of a Hall Thruster Efficiency Analysis," *Journal of Propulsion and Power*, Vol. 25, No. 6, 2009, pp. 1163–1177. https://doi.org/10.2514/1.38092

[13] Shastry, R., Hofer, R. R., Reid, B. M., and Gallimore, A. D., "Method for Analyzing ExB Probe Spectra from Hall Thruster Plumes," *Review of Scientific Instruments*, Vol. 80, No. 6, 2009, Paper 063502. https://doi.org/10.1063/1.3152218

[14] Hofer, R. R., Jankovsky, R. S., and Gallimore, A. D., "High-specific Impulse Hall Thrusters, Part 1: Influence of Current Density and Magnetic Field," *Journal of Propulsion and Power*, Vol. 22, No. 4, 2006, pp. 721–731. https://doi.org/10.2514/1.15952

[15] Brown, D. L., "Investigation of Low Discharge Voltage Hall Thruster Characteristics and Evaluation of Loss Mechanisms," Ph.D. Dissertation, Univ. of Michigan, Ann Arbor, MI, 2009.

[16] Reid, B. M., "The Influence of Neutral Flow Rate in the Operation of Hall Thrusters," Ph.D. Dissertation, Univ. of Michigan, Ann Arbor, MI, 2009.

[17] Huang, W., Shastry, R., Soulas, G. C., and Kamhawi, H., "Farfield Plume Measurement and Analysis on the NASA-300M and NASA-300 MS," *33rd International Electric Propulsion Conference*, Electric Rocket Propulsion Soc. Paper IEPC-2013-057, Fairview Park, OH, 2013.

[18] Chu, E., Goebel, D. M., and Wirz, R. E., "Reduction of Energetic Ion Production in Hollow Cathodes by External Gas Injection," *Journal of Propulsion and Power*, Vol. 29, No. 5, 2013, pp. 1155–1163. https://doi.org/10.2514/1.B34799

[19] Goebel, D. M., and Chu, E., "High-Current Lanthanum Hexaboride Hollow Cathode for High-Power Hall Thrusters," *Journal of Propulsion and Power*, Vol. 30, No. 1, 2014, pp. 35–40. https://doi.org/10.2514/1.B34870

[20] Hall, S. J., Jorns, B. A., Gallimore, A. D., and Goebel, D. M., "Operation of a High-Power Nested Hall Thruster with Reduced Cathode Flow Fraction," *Journal of Propulsion and Power*, Vol. 36, No. 6, Nov. 2020, pp. 912–919.

[21] Dankanich, J. W., Walker, M., Swiatek, M. W., and Yim, J. T., "Recommended Practice for Pressure Measurement and Calculation of Effective Pumping Speed in Electric Propulsion Testing," *Journal of Propulsion and Power*, Vol. 33, No. 3, 2017, pp. 668–680. https://doi.org/10.2514/1.B35478

[22] Haag, T. W., "Thrust Stand for High-Powered Electric Propulsion Devices," *Review of Scientific Instruments*, Vol. 62, No. 5, 1991, pp. 1186–1191. https://doi.org/10.1063/1.1141998

[23] Xu, K. G., and Walker, M. L. R., "High-Power, Null-Type, Inverted Pendulum Thrust Stand," *Review of Scientific Instruments*, Vol. 80, No. 5, 2009, Paper 055103. https://doi.org/10.1063/1.3125626

[24] Polk, J. E., Pancotti, A., Haag, T., King, S., Walker, M., Blakely, J., and Ziemer, J., "Recommended Practice for Thrust Measurement in Electric Propulsion Testing," *Journal of Propulsion and Power*, Vol. 33, No. 3, 2017, pp. 539–555. https://doi.org/10.2514/1.B35564

[25] Hutchinson, I. H., *Principles of Plasma Diagnostics*, 2nd ed., Cambridge Univ. Press, New York, 2002.

[26] Savitzky, A., and Golay, M. J. E., "Smoothing and Differentiation of Data by Simplified Least Squares Procedures," *Analytical Chemistry*, Vol. 36, No. 8, 1964, pp. 1627–1639. https://doi.org/10.1021/ac60214a047

[27] Lobbia, R. B., and Beal, B. E., "Recommended Practice for Use of Langmuir Probes in Electric Propulsion Testing," *Journal of Propulsion and Power*, Vol. 33, No. 3, 2017, pp. 566–581. https://doi.org/10.2514/1.B35531

[28] Lieberman, M. A., and Lichtenberg, A. J., *Principles of Plasma Discharges and Materials Processing*, 2nd ed., Wiley, Hoboken, NJ, 2005.

[29] Peterson, P. Y., Jacobson, D. T., Manzella, D. H., and John, J. W., "The Performance and Wear Characterization of a High-Power High-Isp NASA Hall Thruster," *41st AIAA/SAE/ASEE Joint Propulsion Conference*, AIAA Paper 2005-4243, 2005. https://doi.org/10.2514/6.2005-4243

[30] Mikellides, I. G., and Ortega, A. L., "2D (r-z) Numerical Simulations of the Plasma and Channel Erosion in a 100 kW Class Nested Hall Thruster," *Plasma Sources Science and Technology*, Vol. 27, No. 7, 2018, Paper 075001. https://doi.org/10.1088/1361-6595/aacacb

[31] Randolph, T., Kim, V., Kaufman, H., Kozubsky, K., Zhurin, V. V., and Day, M., "Facility Effects on Stationary Plasma Thruster Testing," *23rd International Electric Propulsion Conference*, Electric Rocket Propulsion Soc. Paper IEPC-1993-093, Fairview Park, OH, 1993.

[32] Hofer, R. R., and Anderson, J. R., "Finite Pressure Effects in Magnetically Shielded Hall Thrusters," *50th AIAA/ASME/SAE/ASEE Joint Propulsion Conference*, AIAA Paper 2014-3709, 2014. https://doi.org/10.2514/6.2014-3709

[33] Kamhawi, H., Haag, T., Huang, W., Herman, D. A., Thomas, R., Shastry, R., Yim, J., Chang, L., Clayman, L., Griffith, C., and Myers, J., "Performance Characterization of the Solar Electric Propulsion Technology Demonstration Mission 12.5-kW Hall Thruster," *34th International Electric Propulsion Conference*, Electric Rocket Propulsion Soc. Paper IEPC-2015-007, Fairview Park, OH, 2015.

[34] Frieman, J. D., "Characterization of Background Neutral Flows in Vacuum Test Facilities and Impacts on Hall Effect Thruster Operation," Ph.D. Dissertation, Georgia Inst. of Technology, Atlanta, GA, 2017.

[35] Frieman, J. D., Liu, T. M., and Walker, M. L., "Background Flow Model of Hall Thruster Neutral Ingestion," *Journal of Propulsion and Power*, Vol. 33, No. 5, 2017, pp. 1087–1101. https://doi.org/10.2514/1.B36269

[36] Cai, C., "Theoretical and Numerical Studies of Plume Flows in Vacuum Chambers," Ph.D. Dissertation, Univ. of Michigan, Ann Arbor, MI, 2005.

[37] Sekerak, M. J., Gallimore, A. D., Brown, D. L., Hofer, R. R., and Polk, J. E., "Mode Transitions in Hall-Effect Thrusters Induced by Variable Magnetic Field Strength," *Journal of Propulsion and Power*, Vol. 32, No. 4, 2016, pp. 903–917. https://doi.org/10.2514/1.B35709

[38] Nakles, M. R., and Hargus, W. A., Jr., "Background Pressure Effects on Ion Velocity Distribution Within a Medium-Power Hall Thruster," *Journal of Propulsion and Power*, Vol. 27, No. 4, 2011, pp. 737–743. https://doi.org/10.2514/1.48027

J. Blandino
Associate Editor